RSC Advances

PAPER

Cite this: *RSC Adv.*, 2020, **10**, 27788

Hollow waxberry-like cobalt–nickel oxide/S,N-codoped carbon nanospheres as a trifunctional electrocatalyst for OER, ORR, and HER†

Qing Zhang,[a] Wenjie Han,[a] Zhixiao Xu,[b] Yinling Li,[a] Lu Chen,[c] Zhengyu Bai, *[a] Lin Yang [a] and Xiaolei Wang *[bc]

Received 10th April 2020
Accepted 8th June 2020

DOI: 10.1039/d0ra03222k

rsc.li/rsc-advances

With the aggravation of the energy crisis, increasing attention has been paid to electrocatalytic technology for renewable energy devices. In particular, the research on catalysts towards the oxygen evolution reaction (OER), oxygen reduction reaction (ORR), and hydrogen evolution reaction (HER) has become more urgent, and the development of multifunctional electrocatalysts has become a research trend. Here we report the synthesis of waxberry-like cobalt–nickel oxide/S,N-codoped carbon hollow nanocomposites as trifunctional catalysts. Uniform cobalt–nickel glycerate solid spheres are first synthesized as the precursor and subsequently chemically transformed into cobalt–nickel oxide/S,N-codoped carbon hollow nanospheres. Benefiting from the synergistic coupling of cobalt–nickel oxide and S,N-codoped carbon nanocomposites, hierarchical porosity and hollow structure, the cobalt–nickel oxide/S,N-codoped carbon nanohybrids exhibit superior trifunctional electrocatalytic activity and durability towards OER, ORR, and HER in alkaline media.

Introduction

In the past decades, the energy crisis and climate change have stimulated the development of renewable energy storage and conversion technologies.[1,2] Among the many, fuel cells,[3,4] metal–air batteries,[5,6] and water splitting devices[7,8] hold great promise, where key processes involved are the oxygen evolution reaction (OER), oxygen reduction reaction (ORR), and hydrogen evolution reaction (HER). Unfortunately, due to the high energy barrier and complex multi-electron transfer, these processes are generally limited by sluggish kinetics, which accordingly requires the use of electrocatalysts.[9,10]

Platinum (Pt)[11] and its alloys[12] exhibit excellent catalytic activity for ORR and HER, whereas ruthenium (Ru)[13] and iridium (Ir)[14] based materials are mostly efficient toward OER in alkaline media. However, the limited reserves and uneven distribution of these noble metals significantly increase the cost of energy devices and thus impede their wide application. Moreover, these precious metals based electrocatalysts often suffer from poor durability due to the deactivation and agglomeration.[15] To address these critical issues, extensive efforts have been made to seek low-cost, highly active and stable alternatives. Especially, earth-abundant transition metal-based catalysts, such as iron (Fe), cobalt (Co), nickel (Ni) and their oxides, sulfides, phosphides, carbides, nitrides, borides, as well as alloys or complex have been intensively studied due to their relatively high availability and low cost.[16] It is reported that the incompletely occupied d-orbitals of these elements facilitate the conversion at various valence states by obtaining and donating electrons with low energy, which provides high activity for electrochemical processes.[17] For example, cobalt/N-doped carbon hollow particles (Co/NC)[18] and sulfur-doped Fe/N/C catalyst (Fe/SNC)[19] were utilized for ORR, Ni–Fe layered double hydroxide (Ni–Fe LDH)[20] and Fe-doped Co_9S_8 nanomicrospheres (Fe-Co_9S_8 NM/NF)[21] for OER, molybdenum-nickel bimetallic carbonitride (MoNiNC)[22] and petaloid FeP[23] for HER.

Compared with mostly reported monofunctional catalysts, bifunctional and even trifunctional catalysts towards ORR, OER, and HER are attracting increasing attention. For instance, the Co_3O_4 nanocrystals embedded nitrogen-doped, partially graphitized carbon framework (Co_3O_4/NPGC)[24] with unique pomegranate-like composite architecture has been shown to remarkably accelerate the ORR and OER process for rechargeable metal–air batteries. Dai's group reported N,P,F-codoped graphene with excellent trifunctional activity towards ORR, OER, and HER, enabling self-powered water splitting device

[a]*Collaborative Innovation Center of Henan Province for Green Manufacturing of Fine Chemicals, Henan Key Laboratory of Boron Chemistry and Advanced Energy Materials, Key Laboratory of Green Chemical Media and Reactions, Ministry of Education, School of Chemistry and Chemical Engineering, Henan Normal University, Xinxiang, Henan 453007, PR China. E-mail: baizhengyu@htu.edu.cn*

[b]*Department of Chemical and Materials Engineering, University of Alberta, Edmonton, Alberta T6G 1H9, Canada. E-mail: xiaolei.wang@ualberta.ca*

[c]*Department of Chemical and Materials Engineering, Concordia University, Montreal, Quebec H3G 1M8, Canada*

† Electronic supplementary information (ESI) available. See DOI: 10.1039/d0ra03222k

with Zn–air as the power source.[25] Nevertheless, the development of trifunctional electrocatalysts remains challenging and should consider following aspects: (i) the selection of suitable material with universal electrocatalytic activity for all of the three reactions; (ii) the effective combination of electrocatalysts with synergistic effect; (iii) the efficient construction of the micro/nano-structure providing not only sufficient and accessible active sites and fast electron transfer pathways but also chemical and electrochemical stability for excellent durability.[26]

Herein, we demonstrate the design and synthesis of cobalt–nickel oxide/S,N-codoped carbon (referred to as $CoNiO_2$/SNC) with a unique architecture of nanoparticle-constructed microspheres, reminiscent of waxberry. As shown in Fig. 1a, the composite material can be fabricated through a two-step synthesis, where Co–Ni glycerate was used as the precursor while thioacetamide and urea were used as the S and N sources. Such a composite material possesses several features that favor the fast and reliable electrocatalytic OER, ORR and HER processes. First, hierarchical porosity can facilitate the electrolyte penetration during electrochemical test; second, the hollow structure with easily accessible and highly exposed active sites enhances the catalyst–electrolyte contact area and offers sufficient space for electrochemical reactions; third, cobalt–nickel double metal oxide and S,N-codoped carbon composite can be combined to complement each other, and then the synergistic coupling of the two enhances the electrocatalytic activity.[27] As such, we believe $CoNiO_2$/SNC hollow nanospheres not only possess improved activity but also excellent stability for OER, ORR and HER.

Experimental section

Materials synthesis

Synthesis of Co–Ni glycerate. In a typical synthesis, $Co(NO_3)_2 \cdot 6H_2O$ (0.25 mmol) and $Ni(NO_3)_2 \cdot 6H_2O$ (0.125 mmol) were dissolved in isopropanol (40 mL). Glycerol (8 mL) was then added to the above mixture to form a transparent light pink solution by stirring. The solution was transferred to a 100 mL Teflon-lined stainless-steel autoclave and kept at 180 °C for 6 h. After naturally cooling down, the brown powder (Co–Ni glycerate) was separated by centrifugation, washed with ethanol several times and dried under vacuum oven at 40 °C.

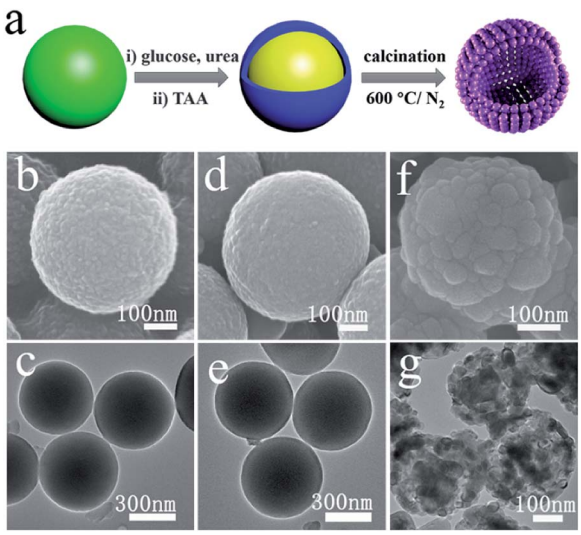

Fig. 1 Schematic illustration of the synthesis of waxberry-like hollow $CoNiO_2$/SNC nanocomposites (a). SEM (b) and TEM (c) images of Co–Ni glycerate precursors; SEM (d) and TEM (e) images of the intermediate products; SEM (f) and TEM (g) images of hollow $CoNiO_2$/SNC nanocomposites.

Synthesis of $CoNiO_2$/SNC hollow nanospheres. Co–Ni glycerate (0.04 g) powder was well dispersed in isopropanol (20 mL) with ultrasonication followed by the addition of glucose aqueous solution (1.0 M, 2.0 mL), isopropanol solution of urea (0.4 M, 20 mL), and glycerol (8 mL) was then added to the above mixture to form a transparent solution by stirring. The transparent solution was transferred to a 100 mL Teflon-lined stainless-steel autoclave and kept at 180 °C for 4 h. The dark brown powder was separated by centrifugation, washed with ethanol and water for several times and dried under vacuum at 40 °C. For the preparation of $CoNiO_2$/SNC nanocomposites, 40 mg of the above dark brown powder and 80 mg thioacetamide (TAA) were added into 32 mL ethanol under a vigorous stirring for 10 min. Then the mixture was heated to 90 °C in a water bath and refluxed for 1 h under stirring. After centrifugation and washing with ethanol for several times, the black powder was obtained. The final product was annealed under N_2 atmosphere at 600 °C for 2 h with a ramp rate 1 °C min^{-1}.

Synthesis of $CoNiO_x$/NC nanocomposites. For comparison, we had prepared $CoNiO_x$/NC, the preparation method was the same as above except that the sulfurization was not carried out.

Characterization

The microstructure and morphology of the prepared catalyst was investigated by a Germany Zeiss SUPRA40 field emission scanning electron microscopy (FESEM) at an operating voltage of 15 kV and JEOL-100CX high resolution transmission electron microscopy (HR-TEM) at an operating voltage of 150 kV. XPS measurements were performed on a PHI 5000C ESCA system. The pore structure was analyzed with N_2 adsorption–desorption measurements on a Brunauer–Emmett–Teller surface area analyzer (Quantachrome Instruments QuadraSorb SI4) and the pore size distribution was obtained by a Barrett–Joyner–Halenda (BJH) model.

Electrochemical measurements

Electrochemical measurements were carried out on a CHI 760E workstation (CH Instruments, Chenhua, Shanghai, China) equipped with a rotating disk electrode in a standard three-electrode cell. A glassy carbon electrode (GC; 5 mm in diameter), a graphite rod, and a saturated calomel electrode (SCE) was used as the working electrode, counter electrode, and the reference electrode, respectively. The potential recorded was converted to the reversible hydrogen electrode (RHE) according to Nernst equation $E_{RHE} = E_{SCE} + 0.059 \times pH + 0.241$. To prepare the sample ink, the electrocatalyst (2.0 mg) was dispersed in isopropanol (485 μL) containing 15 μL 5.0 wt% Nafion solution. The mixture was well dispersed by

ultrasonication for 20 min to obtain homogenous ink. Next, 40 μL of ink was loaded onto the pre-polished RDE surface. The ORR, OER and HER tests were performed in O_2-saturated 0.1 M KOH solutions, N_2-saturated 0.1 M (or 1 M) KOH solutions and N_2-saturated 1 M KOH solutions, respectively. For ORR, polarization curves were recorded from 0.1 to −1.0 V (*vs.* SCE) at a scan rate of 5 mV s^{-1} with a series of rotating electrode speeds (400, 625, 900, 1225, 1600 and 2025 rpm). The kinetic parameters have been calculated by Koutecky–Levich (K–L) equations[28]

$$\frac{1}{J} = \frac{1}{J_L} + \frac{1}{J_K} = \frac{1}{B\omega^{1/2}} + \frac{1}{J_K}$$

$$B = 0.62nFC_0(D_0)^{2/3}\gamma^{-1/6}$$

$$J_K = nFkC_0$$

in which J, J_K, and J_L are the measured current density, kinetic and diffusion-limiting current densities, respectively; ω is the angular velocity of the disk, n is the number of electrons transferred in ORR, F is the Faraday constant (F = 96 485C mol L^{-1}), C_0 is the bulk solubility of O_2, D_0 is diffusion coefficient of O_2, γ is the kinematic viscosity of the electrolyte, and k is the electron transfer rate constant. The number of electrons transferred (n) can be obtained from the slope of the K–L plots.

Linear sweep voltammetry (LSV) for OER and HER were conducted with a scan rate of 5 mV s^{-1} at room temperature. The *iR*-compensation was performed by electrochemical impedance spectroscopy to correct the compensated potential. The LSV curves were replotted as potential (V) *versus* log current (log j) to get Tafel plots for quantification of the OER and HER kinetic performance of as-prepared catalysts. By fitting the linear part of the Tafel plots to obtain the Tafel slope (b) according to the Tafel equation ($V = a + b\log(j)$).[28] Electrochemical double layer capacitance (C_{dl}) was calculated by cyclic voltammetry (CV) at nonfaradaic potential range without polarization current. Then the C_{dl} value has been converted to the electrochemical surface area (ECSA) using the equation ECSA = C_{dl}/C_S (where C_S is the specific capacitance with 0.040 mF cm^{-2} in 1 M KOH electrolyte). Typically, a series of CV curves were recorded at various scan rates (20, 40, 60, 80, 100 mV s^{-1}, *etc.*) in 0.1 to 0.2 V (*vs.* SCE) range.

The stability of catalysts toward ORR, OER, HER was measured by cyclic voltammetry (CV) from 0.0 to −1.0 V (*vs.* SCE) at a scan rate of 50 mV s^{-1}, 0.0 to 0.7 V (*vs.* SCE) at a scan rate of 50 mV s^{-1}, −1 to −1.7 V (*vs.* SCE) at a scan rate of 50 mV s^{-1}, respectively.

Results and discussion

Fig. 1a illustrates the overall synthetic process of waxberry-like hollow $CoNiO_2$/SNC nanocomposites. Firstly, Co–Ni glycerate spheres with an average diameter of 400 nm and a rough surface was obtained by a hydrothermal reaction, as shown in Fig. 1b. The rough surface of Co–Ni glycerate is covered with ultrafine nanoparticles whose diameter is around 10 nm (Fig. S1†). Fig. 1c reveals its solid interior structure. Subsequently, Co–Ni glycerate spheres were treated with glucose, urea, and TAA to achieve carbon coating, nitrogen and sulfur co-doping. Compared with Co–Ni glycerate, the sample after chemical treatment maintains well its spherical morphology and solid interior structure but its surface is smooth (Fig. 1d and e), which can be ascribed to the formation of homogenous and continuous carbon coating on the surface of these microspheres. Lastly, the carbon-coated, N,S-doped, Co–Ni-based microspheres was calcined in flowing N_2 atmosphere at 600 °C for 2 h to obtain $CoNiO_2$/SNC nanocomposites (Fig. 1f and g). For comparison, carbon-coated, N-doped, Co–Ni-based nanocomposites, denoted as $CoNiO_x$/NC, were also synthesized by the same procedure except without the TAA-treatment.

The representative SEM image of $CoNiO_2$/SNC in Fig. 2a indicates that as-synthesized nanocomposites exhibit a similar spherical morphology but with a smaller diameter of around 300 nm than samples without annealing. The high-magnification SEM image (Fig. 1f) shows that the nanocomposites are constructed by nanoparticles with a size of *ca.* 60 nm, which looks like waxberry fruit. In stark contrast to samples without annealing, the $CoNiO_x$/SNC also possess a hollow structure (Fig. 2b), which provides not only extra active sites but also faster access to the abundant active sites of the electrocatalysts.[26] Such a waxberry-like hollow architecture is further revealed by TEM images (Fig. 2c), which clearly show the nanoparticle-constructed microspheres with a hollow interior, consistent with SEM observations. Fig. 2d shows the high-angle annular dark-field (HAADF) scanning TEM (STEM) image of a single $CoNiO_2$/SNC nanocomposite sphere. The hollow structure is well defined, while the corresponding energy-dispersive X-ray spectroscopy (EDS) mapping result (Fig. 2e) confirms the presence of elements Co, Ni, O, C, N and S with homogeneous dispersion. In particular, the existence of N, S implies the successful N,S doping through the whole $CoNiO_2$/SNC nanocomposites. The high-resolution TEM (HRTEM) image in Fig. 2f shows clear crystal lattice $CoNiO_2$ nanoparticles with an average interplanar spacing of 0.244 nm. The X-ray

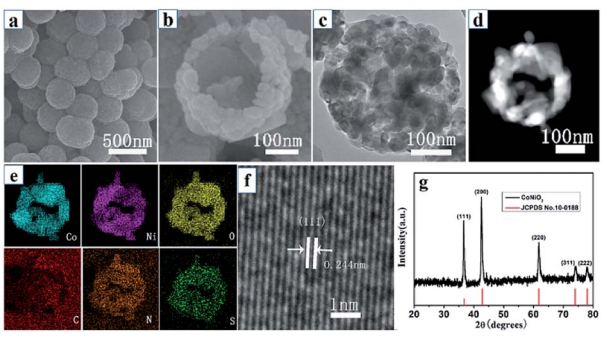

Fig. 2 SEM (a and b), TEM (c) and HAADF-STEM (d) images of the $CoNiO_2$/SNC nanocomposites and corresponding EDX mappings (e) of Co, Ni, O, C, N and S elements. (f) HRTEM image of a single $CoNiO_2$/SNC nanoparticle. (g) XRD pattern of the $CoNiO_2$/SNC nanocomposites.

diffraction (XRD) pattern of the nanocomposites in Fig. 2g can be indexed to a cubic crystal structure (JCPDS No. 10-0188), indicating the formation of highly crystalline $CoNiO_2$, where the (111) plane is well exposed, which is consistent with the HRTEM result. As the control sample, $CoNiO_x$/NC has a similar morphology to $CoNiO_2$/SNC except that the particles of $CoNiO_x$/NC are adhered to each other (Fig. S2†), and XRD (Fig. S3†) also confirms that the control sample is cobalt–nickel oxide nanocomposites.

To further understand the porosity of $CoNiO_2$/SNC, N_2 adsorption and desorption measurements were conducted. As shown in Fig. 3a, a type-IV isotherm is obtained, suggesting the coexistence of mesopores and macropores.[24] The specific surface area of the $CoNiO_2$/SNC nanocomposites is calculated to be 22.1842 $m^2\ g^{-1}$ based on the Brunauer–Emmett–Teller (BET) analysis of the nitrogen absorption desorption isotherms. The pore size distribution (Fig. 3b) confirms again the hierarchically porous structure that is probably originated from the assembly of small nanoparticles. X-ray photoelectron spectroscopy (XPS) was used to detect the chemical composition of the $CoNiO_2$/SNC nanocomposites. The survey spectrum (Fig. S4a†) shows the presence of Co, Ni, O, C, N and S elements for the nanocomposites. The high-resolution C 1s spectra was showed in Fig. S4b.†The peaks at 284.5, 286.6 and 288.3 eV correspond to C–C, C–O and C=O bonds, respectively. The binding energy peaks at 284.1 and 285.5 eV are assigned to C–S and C–N, which further indicates the N/S-doping in $CoNiO_2$/SNC hollow nanospheres. As shown in Fig. S4c,† the N 1s existed in the form of pyrrolic N (400.2 eV) and oxidic N (402.3 eV), which would play crucial role in the ORR performances.[29] In the Ni 2p region in Fig. 3c, the two peaks at 873.2 and 855.4 eV are attributed to Ni $2p_{1/2}$ and $2p_{3/2}$ for Ni(II), respectively, along with two shakeup satellites (Sat.). In Fig. 3d, the two peaks centered at 796.4 and 780.7 eV can be assigned to Co $2p_{1/2}$ and Co $2p_{3/2}$, respectively, and the two weak shoulder peaks at 802.9 and 786.3 eV are the corresponding satellite peaks, confirming the existence of Co(II). As shown in Fig. 3e, the peak at 168.2 eV is attributed to SO_4^{2-}, arising from the partly oxidized sulfur species (C–SO_4).[30] Finally, the core-level O 1s spectrum (Fig. 3f) shows three fitting peaks, which are attributed to Ni–O, Co–O and excessive oxygen-containing groups (such as, –OH and C–O) on the sample surface, respectively.[31]

Possessing waxberry-like hollow architecture with hierarchical porosity, S,N-codopant, and strong carbon coupling, $CoNiO_2$/SNC is promising for various electrocatalysis. The electrocatalytic performances of $CoNiO_2$/SNC, $CoNiO_x$/NC and RuO_2 towards oxygen evolution reaction (OER) were firstly tested in a three-electrode system with 0.1 M KOH as the electrolyte. The linear sweep voltammetry (LSV) curves illustrate that $CoNiO_2$/SNC requires the overpotentials of only around 381 mV to deliver the current densities of 10 mA cm^{-2} (Fig. 4a), which is much lower than those of $CoNiO_x$/NC (429 mV) and RuO_2 (490 mV). Fig. 4b manifests that the Tafel slope for $CoNiO_2$/SNC is 34 mV dec^{-1}, smaller than that of $CoNiO_x$/NC (64 mV dec^{-1}) and RuO_2 (109 mV dec^{-1}), indicating the faster OER kinetics of $CoNiO_2$/SNC. It is worth mentioning that $CoNiO_2$/SNC shows superior activity to the precious metal-based catalysts (RuO_2), implying its high applicability. In addition, the OER performance of the three samples were tested in 1 M KOH. Although the same activity trend of three catalysts, a better catalytic activity was obtained in 1 M KOH. The overpotential and Tafel slope for $CoNiO_2$/SNC, $CoNiO_x$/NC and RuO_2 are 280 mV, 335 mV, 329 mV, 55 mV dec^{-1}, and 58 mV dec^{-1}, 72 mV dec^{-1}, respectively (Fig. 4d and e). Such an exceptional OER activity of $CoNiO_2$/SNC is comparable and even superior to recently reported OER catalysts (Table S1†). Besides, cyclic voltammetry (CV) measurements at different sweep speed were performed to investigate the electrochemically active surface area (ECSA) of the sample. In the potential range from 1.1 to 1.2 V, there is not faradaic current observed (Fig. S5a and b†). According to the linear relationship between current density and scan rates (Fig. S5c†), the C_{dl} values of the $CoNiO_2$/SNC and $CoNiO_x$/NC are calculated to be 68.78 and 40.25 mF, respectively. Therefore, it is concluded that the ECSA of $CoNiO_2$/SNC is much larger than $CoNiO_x$/NC. It shows that there are more active sites exposed in $CoNiO_2$/SNC, which greatly improves the performance of OER. Subsequently, durability of $CoNiO_2$/SNC for water oxidation in both 0.1 M and 1 M KOH were measured by cyclic voltammetry (CV). As shown in Fig. 4c and f, $CoNiO_2$/SNC manifests only negligible current loss even after 1000 cycles.

Next, the electrocatalytic ORR performance of the $CoNiO_2$/SNC catalyst was studied. Cyclic voltammetry (CV)

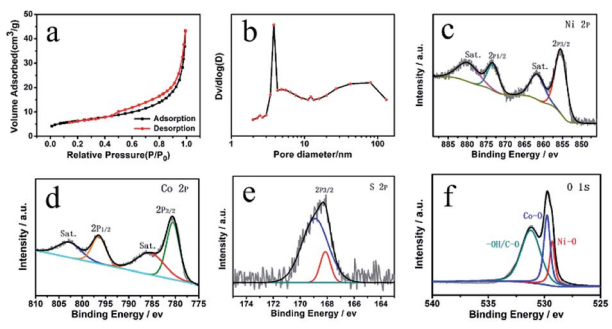

Fig. 3 N_2 adsorption/desorption isotherms (a) and pore size distribution (b) of the $CoNiO_2$/SNC nanocomposites. High resolution XPS spectra of element Ni (c), Co (d), S (e) and O (f) in the nanocomposites.

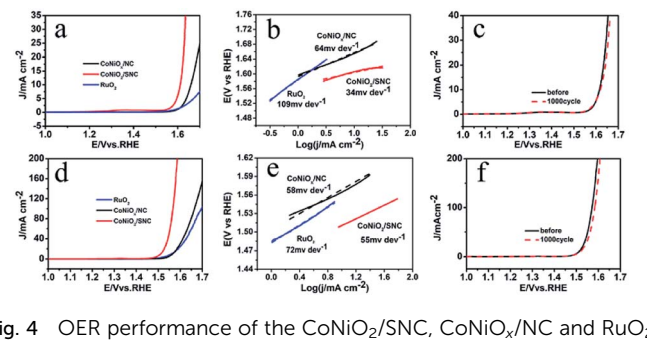

Fig. 4 OER performance of the $CoNiO_2$/SNC, $CoNiO_x$/NC and RuO_2 catalysts in an N_2-saturated in (a–c) 0.1 M or (d–f) 1 M KOH solution. (a and d) Polarization curves and (b and e) Tafel plots of the three catalysts; (c and f) stability tests of the $CoNiO_2$/SNC catalyst.

measurements were initially carried out in a conventional three-electrode electrochemical cell in an O_2- or N_2-saturated 0.1 M KOH solution. In the absence of oxygen, no redox peaks were observed for $CoNiO_2$/SNC and $CoNiO_x$/NC (Fig. 5a). By contrast, apparent cathodic peaks at 0.59 V (*versus* reversible hydrogen electrode, RHE) were detected in O_2-saturated solution, indicating the electrocatalytic activity of $CoNiO_2$/SNC and $CoNiO_x$/NC. Moreover, the peak current density of $CoNiO_2$/SNC is higher than $CoNiO_x$/NC, suggestive of a better electrocatalytic activity of $CoNiO_2$/SNC. To further evaluate the ORR performance of the $CoNiO_2$/SNC, rotating disk electrode tests were performed in O_2-saturated 0.1 M KOH at a rotation rate of 1600 rpm. Fig. 5b shows that the waxberry-like hollow $CoNiO_2$/SNC nanocomposites exhibit more positive onset and half-wave potentials (0.85 and 0.70 V, respectively) than those of the $CoNiO_x$/NC (0.845 and 0.67 V, respectively). Also, the diffusion-limiting current density of $CoNiO_x$/SNC is 6.5 mA cm^{-2}, which is higher than that of $CoNiO_x$/NC (5.4 mA cm^{-2}), confirming the superior activity of $CoNiO_2$/SNC to $CoNiO_2$/NC. Of note, the high catalytic activity of $CoNiO_2$/SNC is comparable and even superior to recently reported non-precious metal ORR catalysts, such as Fe_2N-NGC1-1000 (0.83 and 0.66 V *vs.* RHE)[31], $NiCo_2O_4$-rGO (0.85 and 0.58 V *vs.* RHE)[32] and hollowed-out $MnCo_2O_{4.5}$ nanocages (0.8 and 0.7 V *vs.* RHE).[33] To investigate the ORR kinetics of the $CoNiO_2$/SNC electrocatalyst, polarization curves were obtained at various rotation speeds ranging from 400 to 2025 rpm with a scan rate of 5 mV s^{-1}. As shown in Fig. 5c, the $CoNiO_2$/SNC exhibited a well-defined platform of diffusion-limiting currents at all rotational speeds. Derived from Fig. 5c, K–L plots were obtained (Fig. 5c inset), showing good linearity at various potentials in the mass-transport-limited region (0.2–0.5 V *vs.* RHE, Fig. 5c), suggesting the first-order reaction kinetics with respect to oxygen. According to the calculation, the number of electron transfer is close to 4 (Fig. S6†), indicating a four electron transfer process from the reduction of O_2 to the formation of H_2O. Subsequently, the stability of $CoNiO_2$/SNC catalyst in 0.1 M KOH was measured by cyclic voltammetry (CV). The $CoNiO_2$/SNC catalyst exhibits excellent stability towards the ORR without significant losses in activity after 6000 cycles (Fig. S7†). Apart from the bifunctional catalysis toward ORR and OER, the $CoNiO_2$/SNC catalyst also displays good performance for HER. According to the polarization curves (Fig. 5d), a decent HER catalytic activity can be achieved for the $CoNiO_2$/SNC catalyst which has an onset potential of about 0.23 V as well as a overpotential of around 330 mV at the current density of 10 mA cm^{-2}. Derived from polarization curves, Tafel curves (Fig. 5e) showcase the Tafel value of $CoNiO_2$/SNC is 101 mV dec^{-1}, implying HER behavior proceeds *via* a Volmer–Tafel mechanism with electrochemical desorption of hydrogen as the rate-limiting step. These values (onset potential, overpotential and Tafel slope) of $CoNiO_2$/SNC are much lower than those of control sample, again substantiating the superior catalytic activity of $CoNiO_2$/SNC. Fig. 5f show the stability test for HER. $CoNiO_2$/SNC manifests only negligible current loss even after 1000 cycles. The above results show that $CoNiO_2$/SNC nanocomposites catalyst possesses excellent trifunctional electrocatalytic activity towards the ORR, OER and HER.

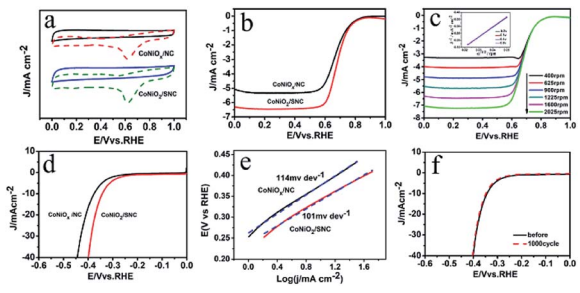

Fig. 5 (a) CV of the $CoNiO_x$/NC and $CoNiO_2$/SNC nanocomposites electrodes in an O_2 and N_2-saturated in 0.1 M KOH solution. (b) ORR polarization curves of the two electrodes at 1600 rpm. (c) ORR polarization curves of the $CoNiO_2$/SNC nanocomposites catalyst at different rotating speeds, with K–L plots at different potentials inset. HER performance of the $CoNiO_2$/SNC and $CoNiO_x$/NC catalysts in N_2-saturated 1 M KOH solution. (d) Polarization curves and (e) Tafel plots of the two catalysts; (f) stability tests of the $CoNiO_2$/SNC catalyst.

After the stability test, hollow waxberry-like $CoNiO_2$/SNC nanocomposites were again characterized by SEM and TEM. The results are shown in Fig. S8.† The SEM and TEM images show that the morphology and structure of the sample did not change significantly after the stability test. The results show that this hollow waxberry-like $CoNiO_2$/SNC nanocomposites have excellent stability.

Conclusions

In summary, we have successfully developed, for the first time, $CoNiO_2$/SNC nanocomposites with the unique waxberry-like hollow architecture as trifunctional electrocatalysts towards OER, ORR, and HER. Benefiting from its unique hierarchical porosity, hollow structure and the strongly coupling of $CoNiO_2$ and N,S-codoped carbon, the $CoNiO_2$/SNC electrocatalyst manifests excellent activity and good stability for OER, ORR, and HER in alkaline media. Furthermore, our approach may be further applied to other transition metal oxide, sulfides, phosphides, and nitrides with carbon coating and heteroatom-doping, thus opening a new avenue for constructing multifunctional electrocatalysts and electrodes in fuel cells, metal–air battery, and water splitting.

Conflicts of interest

There is no conflict of interest to declare.

Acknowledgements

This work was financially supported by the National Natural Science Foundation of China (Grant No. 51922008 and 51872075), the 111 Project (Grant No. D17007), Henan Center for Outstanding Overseas Scientists (Grant No. GZS2018003).

Notes and references

1 D. U. Lee, P. Xu, Z. P. Cano, A. G. Kashkooli, M. G. Park and Z. Chen, *J. Mater. Chem. A*, 2016, **4**(19), 7107–7134.

2 Z. Bai, S. Li, J. Fu, Q. Zhang, F. Chang, L. Yang, J. Lu and Z. Chen, *Nano Energy*, 2019, **58**, 680–686.
3 V. Bernales, M. A. Ortuno, D. G. Truhlar, C. J. Cramer and L. Gagliardi, *ACS Cent. Sci.*, 2018, **4**(1), 5–19.
4 L. Xue, Y. Li, X. Liu, Q. Liu, J. Shang, H. Duan, L. Dai and J. Shui, *Nat. Commun.*, 2018, **9**(1), 3819.
5 F. Meng, H. Zhong, D. Bao, J. Yan and X. Zhang, *J. Am. Chem. Soc.*, 2016, **138**(32), 10226–10231.
6 M. Jahan, Z. Liu and K. P. Loh, *Adv. Funct. Mater.*, 2013, **23**(43), 5363–5372.
7 J. Yang, X. Wang, B. Li, L. Ma, L. Shi, Y. Xiong and H. Xu, *Adv. Funct. Mater.*, 2017, **27**(17), 1606497.
8 J. Yin, Y. Li, F. Lv, M. Lu, K. Su, W. Wang, L. Wang, F. Cheng, Y. Li, P. Xi and S. Guo, *Adv. Mater.*, 2017, **29**(47), 1704681.
9 F. Cheng and J. Chen, *Chem. Soc. Rev.*, 2012, **41**(6), 2172–2192.
10 Y. Jiao, Y. Zheng, M. Jaroniec and S. Z. Qiao, *Chem. Soc. Rev.*, 2015, **44**(8), 2060–2086.
11 T. Yu, D. Y. Kim, H. Zhang and Y. Xia, *Angew. Chem., Int. Ed. Engl.*, 2011, **50**(12), 2773–2777.
12 Z. Peng and H. Yang, *J. Am. Chem. Soc.*, 2009, **131**, 7542–7543.
13 Y. Lee, J. Suntivich, K. J. May, E. E. Perry and Y. Shao-Horn, *J. Phys. Chem. Lett.*, 2012, **3**(3), 399–404.
14 B. Chen, X. He, F. Yin, H. Wang, D. Liu, R. Shi, J. Chen and H. Yin, *Adv. Funct. Mater.*, 2017, **27**(37), 1700795.
15 Y. Gorlin and T. F. Jaramillo, *J. Am. Chem. Soc.*, 2010, **132**, 13612–13614.
16 Y. Gong, Z. Xu, H. Pan, Y. Lin, Z. Yang and X. Du, *J. Mater. Chem. A*, 2018, **6**(12), 5098–5106.
17 J. Zhang and L. Dai, *Angew. Chem., Int. Ed.*, 2016, **55**(42), 13296–13300.
18 B. Y. Guan, L. Yu and X. W. D. Lou, *Adv. Sci.*, 2017, **4**(10), 1700247.
19 H. Shen, E. Gracia-Espino and J. Ma, *Angew. Chem., Int. Ed. Engl.*, 2017, **56**(44), 13800–13804.
20 L. Yu, J. F. Yang, B. Y. Guan, Y. Lu and X. W. D. Lou, *Angew. Chem., Int. Ed. Engl.*, 2018, **57**(1), 172–176.
21 W. Gao, J. Qin, K. Wang, K. Yan, Z. Liu, J. Lin and B. Dong, *Appl. Surf. Sci.*, 2018, **454**, 46–53.
22 F. Wang, Y. Sun, Y. He, L. Liu, J. Xu, X. Zhao, G. Yin, L. Zhang, S. Li, Q. Mao, Y. Huang, T. Zhang and B. Liu, *Nano Energy*, 2017, **37**, 1–6.
23 F. Wang, X. Yang, B. Dong, X. Yu, H. Xue and L. Feng, *Electrochem. Commun.*, 2018, **92**, 33–38.
24 G. Li, X. Wang, J. Fu, J. Li, Y. Zhang, M. G. Park and Z. Chen, *Angew. Chem., Int. Ed.*, 2016, **55**(16), 4977–4982.
25 J. Zhang and L. Dai, *Angew. Chem., Int. Ed.*, 2016, **55**, 13296–13300.
26 D. U. Lee, H. W. Park, M. G. Park, V. Ismayilov and Z. Chen, *ACS Appl. Mater. Interfaces*, 2015, **7**(1), 902–910.
27 F. Kong, X. Fan, A. Kong, Z. Zhou, X. Zhang and Y. Shan, *Adv. Funct. Mater.*, 2018, **28**(51), 1803973.
28 K. Zhang, C. Qu and Z. Liang, *ACS Appl. Mater. Interfaces*, 2018, **10**(36), 30460–30469.
29 W. Fang, H. Hu, T. Jiang, G. Li and M. Wu, *Carbon*, 2019, **146**, 476–485.
30 Z. Hong, Y. Zhen, Y. Ruan, M. Kang, K. Zhou, J. Zhang, Z. Huang and M. Wei, *Adv. Mater.*, 2018, 1802035.
31 Z. Wang, J. Yin, Z. Zhao, Y. Zhang, G. Pang, X. Sun, J. Zhang and C. Yuan, *J. Alloys Compd.*, 2019, **779**, 81–90.
32 G. Zhang, B. Y. Xia, X. Wang and X. W. David Lou, *Adv. Mater.*, 2014, **26**(15), 2408–2412.
33 Z. Bai, J. Heng, Q. Zhang, L. Yang and F. Chang, *Adv. Energy Mater.*, 2018, 1802390.